

---

# GARLIC: GAussian Representation LearnIng for spaCe partitioning

---

Panagiotis Rigas<sup>1,2\*</sup> Panagiotis Drivas<sup>1,4</sup> Charalambos Tzamos<sup>3,4</sup>

Ioannis Chamodrakas<sup>1,4</sup> George Ioannakis<sup>4</sup>

Leonidas J. Guibas<sup>5</sup> Ioannis Z. Emiris<sup>1,2</sup>

<sup>1</sup> Dept. of Informatics & Telecommunications, National and Kapodistrian University of Athens

<sup>2</sup> Archimedes, Athena Research Center

<sup>3</sup> Visual Recognition Group, Faculty of Electrical Engineering, Czech Technical University in Prague

<sup>4</sup> Institute for Language and Speech Processing, Athena Research Center

<sup>5</sup> Stanford University

## Abstract

We introduce GARLIC (GAussian Representation LearnIng for spaCe partitioning), a novel indexing structure based on  $N$ -dimensional Gaussians for efficiently learning high-dimensional vector spaces. Our approach is inspired from Gaussian splatting techniques, typically used in 3D rendering, which we adapt for high-dimensional search and classification. We optimize Gaussian parameters using information-theoretic objectives that balance coverage, assignment confidence, and structural and semantic consistency. A key contribution is to progressively refine the representation through split and clone operations, handling hundreds of dimensions, thus handling varying data densities. GARLIC offers the fast building times of traditional space partitioning methods (e.g., under  $\sim 5$  min build time for SIFT1M) while achieving  $\sim 50\%$  Recall10@10 in low-candidate regimes. Experimental results on standard benchmarks demonstrate our method’s consistency in (a)  $k$ -NN retrieval, outperforming methods, such as Faiss-IVF, in fast-recall by using about half their probes for the same Recall10@10 in Fashion-MNIST, and (b) in classification tasks, beating by  $\sim 15\%$  accuracy other majority voting methods. Further, we show strong generalization capabilities, maintaining high accuracy even with downsampled training data: using just 1% of the training data returns  $\sim 45\%$  Recall@1, thus making GARLIC quite powerful for applications requiring both speed and accuracy.

## 1 Introduction

Let  $X = \{x_i\}_{i=1}^n \subset \mathbb{R}^d$  be a set of high-dimensional embeddings, derived from handcrafted descriptors (e.g., SIFT1M [37]) or learned via neural networks, which encode semantic and geometric similarity. Such embeddings are commonly used in tasks such as  $k$ -nearest neighbor ( $k$ -NN) retrieval and classification. In retrieval, the goal is to return the  $k$  closest points in  $X$  to a query  $q \in \mathbb{R}^d$ , i.e.,  $\mathcal{N}_k(q) = \arg \min_{S \subset X, |S|=k} \sum_{x \in S} \|q - x\|^2$ , typically under Euclidean or cosine distance [2]. For classification, each point  $x \in X$  carries a label  $y_x \in \mathcal{Y}$ , and the query’s

---

\*Correspondence to panagiotis.rigas@athenarc.gr

label is predicted via majority vote among neighbors:  $\hat{y}(q) = \arg \max_{c \in \mathcal{Y}} \sum_{x \in \mathcal{N}_k(q)} \mathbb{I}[y_x = c]$ , where  $\mathbb{I}[\cdot]$  is the indicator function [12]. Alternatively, a learned decision function  $f : \mathbb{R}^d \rightarrow \mathcal{Y}$  can be trained directly over the embedding space [23]. In both cases, the density, structure, and discriminative power of  $X$  are crucial to performance.

Approaches that build a static index, such as hashing techniques [25], and vector quantization methods [19], which partition a set of data points  $X$ , construct the index independently of the data distribution. Rather than fitting the indexing structure to the spatial and geometric properties of set of data point  $X$ , these methods project the data points to a pre-defined and fixed structure. Such methods usually impose generic assumptions on the distribution of  $X$ , to provide theoretical error bound guarantees. Partitions based on such assumptions often misalign with underlying high-dimensional data distributions, which is also known as the *curse of clustering*, while distance metrics fall short due to *curse of dimensionality*.

Several ANN methods build indices aligned with the data distribution, including LSH variants [14, 5], quantization-based approaches [19, 15], clustering methods [6], and tree-based partitioning [31]. These techniques aim to accelerate retrieval by organizing the space into regions aligned with approximate neighborhood structure. While effective in certain regimes, they exhibit key limitations: high training cost for large-scale data, fragile performance under distribution shift, and rigid, non-adaptive structure post-training. In contrast, deep learning methods model the data manifold directly, capturing local density and semantic continuity to enable flexible, unified retrieval and classification [9, 45].

This begs the question: *How can we efficiently learn the high dimensional space to perform fast, accurate and semantic approximate nearest neighbor searches?* In other words can we learn a geometric representation  $\mathcal{G}_\theta$  of  $\mathbb{R}^d$ , parameterized by, e.g., Gaussians or neural fields, that enables efficient, robust solutions to both retrieval and classification, while adapting to the structure and distribution of  $X$ ?

## 1.1 Related Work

**Traditional ANNS approaches.** Approximate nearest neighbor search (ANNS) methods traditionally fall into three categories: (i) *Indexing*, including LSH-based hashing [25, 19, 46], randomized projections and Johnson–Lindenstrauss-based embeddings [4], vector quantization [20, 26, 3], and tree-based methods [28]; (ii) *Sketching*, which compresses data via hash functions to accelerate approximate distance computations [16, 35, 36, 34, 13, 27, 43]; and (iii) *Graph-based search*, which performs greedy traversal on structures such as Navigating Spreading-out Graphs [18] or Hierarchical Navigable Small World Graphs [38]. While effective in practice, these methods typically rely on fixed partitions or hand-crafted heuristics that do not adapt to the geometry of learned embedding spaces.

The rise of high-dimensional embeddings from deep and geometric representation learning has shifted the focus of ANNS toward *learning-based* approaches. In contrast to classical features, these embeddings are structured: they reflect semantic similarity, lie on low-dimensional manifolds, and exhibit highly nonuniform density. This calls for indexing methods that do not impose rigid, predefined partitions, but instead *learn* representations that align with the intrinsic geometry of the data.

**Learning-based indexing.** A prominent direction is *learning to index*, where models are trained to build adaptive partitions over the data [14, 21]. Neural LSH [14], for example, learns a partitioning of  $\mathbb{R}^d$  via a classifier trained on a balanced  $k$ -NN graph. However, such balance constraints often conflict with real data distributions—especially under long-tailed or clustered regimes—leading to poor locality. Beyond hard partitioning, recent approaches have explored classification-based routing [24] and neural scoring of clusters [11], aiming to improve query-time ranking. Yet these methods still rely on discretized, often rigid space decompositions. In contrast, we advocate for a *geometric learning* perspective: learning smooth, structure-aware representations that are density and semantic aligned. Such representations enable unified treatment of retrieval and classification, generalize under distribution shift.

**Contributions.** We propose **GARLIC**, a method for learning geometry-aware representations of high-dimensional spaces via a set of Gaussians optimized for both approximate

nearest neighbor retrieval and classification. GARLIC learns a probabilistic representation that adapts to local data density and semantic similarity, aligning the shape and placement of Gaussians with the underlying structure of the data. In particular, our method adapts to regions with varying intrinsic dimensionality (e.g., curves, surfaces, volumes), enabling each Gaussian to act as an informative geometric primitive and local manifold approximator, rather than a static partitioning cell.

- We introduce a geometric representation learning approach inspired by Gaussian Splatting [30], that implicitly partitions the input space, optimized for both retrieval and classification using a unified training objective.
- We develop adaptive refinement strategies (split, clone) tailored for high-dimensional spaces, and a localized quantization method for handling density variation, improving search efficiency and robustness w.r.t. noise.
- We design a novel information-theoretic objective combining Mahalanobis-based divergence, entropy-reducing confidence, and geometry-preserving anchoring, aligning the Gaussian structure with the data manifold.
- We benchmark GARLIC for retrieval and classification. Our approach exhibits state-of-the-art performance on both tasks w.r.t. runtime-recall tradeoff, especially for small candidate sets. The source code of our approach will be publicly available.

## 2 Method

GARLIC uses a set of  $d$ -dimensional Gaussians  $\mathcal{G} = \{\mathcal{N}(\mu_i, \Sigma_i)\}_i$ , that adapt to the underlying data distribution, provided as a set of points  $x \in X \subset \mathbb{R}^d$ , to represent high-dimensional space for efficient ANNS and classification. We choose Gaussians because they capture both local geometry and statistical structure, unlike simpler volumes such as boxes or zonotopes, and express anisotropy, curvature, and density variation in a unified, continuous form. The closed form Mahalanobis scoring and differentiability also make them well-suited for end-to-end optimization. Starting with data points, we represent the space with the set of Gaussians  $\mathcal{G}$  parameterized by means and covariance matrices via Cholesky decomposition (Sec. 2.1). We optimize the coefficients (mean and cholesky) of the Gaussians using objectives that aim to balance coverage, point assignment confidence, and structural consistency (Sec. 2.2). Unlike traditional partitioning methods that enforce or tend towards balanced divisions [14, 19, 6, 31, 1, 41, 39], our approach adaptively refines the set of Gaussians  $\mathcal{G}$  through splitting and cloning operations, creating a data-dependent partitioning that accommodates varying densities (Sec. 2.3). To further enhance search efficiency, i.e., narrow down the number of searches, a local hyper-spherical quantization index within each Gaussian bucket (Sec. 2.4) is built. At query time, our method uses Mahalanobis distances for fast bucket selection and prioritized bin search for efficient retrieval (Sec. 2.5). This combination of techniques allows GARLIC to effectively capture the natural clustering structure of high-dimensional data while maintaining search performance, as illustrated in Fig. 1.

### 2.1 Gaussian Parameterization

Each Gaussian  $g_i$  is defined by its mean  $\mu_i \in \mathbb{R}^d$  and covariance matrix  $\Sigma_i \in \mathbb{R}^{d \times d}$ , parameterized as  $\Sigma_i = \mathbf{L}_i \mathbf{L}_i^\top$ ,  $\mathbf{L}_i \in \mathbb{R}^{d \times d}$  being a lower triangular Cholesky factor of matrix  $\Sigma_i$ , ensuring positive semi-definiteness (a requirement for valid Gaussian distributions). The means  $\mu_i$  are initialized using K-Means++ [7] on a subset of the training set. Cholesky factors  $\mathbf{L}_i$  are initialized as:

$$\mathbf{L}_i = \log(\bar{\delta}_{\mathcal{E}}) \cdot \mathbf{I}_d + \epsilon,$$

where  $\mathbf{I}_d \in \mathbb{R}^{d \times d}$  is the identity matrix, and  $\bar{\delta}_{\mathcal{E}}$  is the mean Euclidean distance from each  $\mu_i$  to its three nearest neighbors. This ensures that the initial scale of each Gaussian reflects the local data density. The perturbation  $\epsilon \in \mathbb{R}^{d \times d}$  is a random lower-triangular matrix, defined below:

$$\epsilon_{jk} = \begin{cases} 2 \cdot \sigma(r_{jk}) - 1, & j > k \\ 0, & \text{otherwise} \end{cases}$$

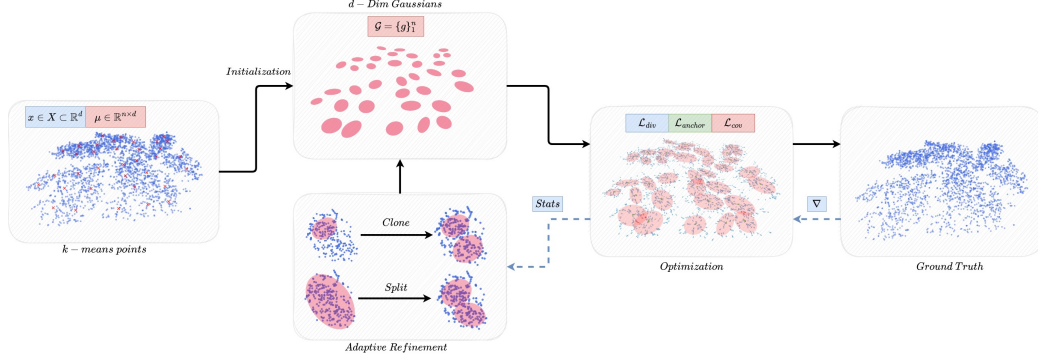


Figure 1: Overview of GARLIC. The method starts with input vector points that are used to initialize a set of Gaussians parameterized by mean  $\mu$  and covariance matrices via Cholesky decomposition. During optimization, these Gaussians are refined through our novel objectives that balance coverage, assignment confidence, and structural consistency. The representation is adaptively improved through split and clone operations creating a data-dependent semantic partitioning that better reflects varying data densities in different regions of the feature space.

where  $r_{jk} \sim \mathcal{U}(0, 0.01)$  and  $\sigma(\cdot)$  is the sigmoid function. This results in diagonal-dominant  $\mathbf{L}_i$ , which stabilizes the optimization process while enabling flexible, anisotropic covariance structures. This initialization strategy attempts to align the initial Gaussian scales with the local data density and to ensure sufficient diversity among Gaussians for adaptive refinement in later stages.

## 2.2 Optimization Objective

We adapt ideas from 3D Gaussian Splatting (3DGS) [29] to high-dimensional nearest neighbor search. While 3DGS performs well in 3D scene modeling, its reliance on Structure-from-Motion (SfM) initialization and view-space heuristics breaks down in high dimensions, where geometry is abstract and dimensions encode heterogeneous features. Splitting and cloning based on spatial cues become unreliable, and optimization suffers in sparse regions. These issues are exacerbated by the curse of dimensionality and clustering, which degrade distance metrics and make balanced partitioning ineffective. High-dimensional indexing demands adaptive, data-aware refinement, something 3DGS heuristics cannot provide.

To handle these issues, inspired by Self-Supervised learning techniques [9, 45], that use information theoretic objectives to increase the capacity of the representation space, we introduce similar information objectives to guide optimization towards a more informative and balanced solution without excessive prior usage. More specifically, we introduce a divergence-based objective that acts as a reconstruction loss, and regularize it to prevent information explosion (i.e., uncontrolled growth and excessive overlap of Gaussians). The divergence loss  $\mathcal{L}_{\text{div}}$  is defined as:

$$\mathcal{L}_{\text{div}} = \frac{1}{N} \sum_{\mathbf{x} \in \mathcal{X}} \left( \min_{g_i \in \mathcal{G}} \delta_M(\mathbf{x}, g_i) - \tau \right)^+,$$

where  $\delta_M(\mathbf{x}, g_i) = \|\mathbf{L}_i^{-1}(\mathbf{x} - \mu_i)\|_2$  denotes the Mahalanobis distance,  $(\cdot)^+ = \max(0, \cdot)$  and  $\tau$  is a standard deviation threshold. It penalizes points that fall outside a Gaussian’s coverage radius ( $\delta_M(\mathbf{x}_i, g_i) > \tau$ ), encouraging Gaussians to expand and cover these points, while points inside ( $\delta_M(\mathbf{x}_i, g_i) \leq \tau$ ) do not contribute, allowing controlled expansion but preventing infinite growth.

Still, Gaussians can overlap, leading to redundant information. To surpass this issue, and mitigate fuzzy assignments of points to Gaussians, we introduce a covariance-based regularization, which encourages each Gaussian to dominate its assigned points. Specifically,

given a point  $\mathbf{x}$ , we define its coverage set, i.e., the set of Gaussians that satisfy the coverage radius constraint, as  $\mathcal{M}(\mathbf{x}) = \{g_i \in \mathcal{G} \mid \delta_M(\mathbf{x}, g_i) \leq \tau\}$ .

Then, we compute the normalized soft-assignment probabilities based on Euclidean distances ( $\delta_{\mathcal{E}}$ ) as  $p_i(\mathbf{x}) = e^{-\delta_{\mathcal{E}}(\mathbf{x}, \mu_i)} / \sum_{g_j \in \mathcal{M}(\mathbf{x})} e^{-\delta_{\mathcal{E}}(\mathbf{x}, \mu_j)} + \epsilon$ ,  $\forall g_i \in \mathcal{M}(\mathbf{x})$ . The covariance loss  $\mathcal{L}_{\text{cov}}$  is defined as:

$$\mathcal{L}_{\text{cov}} = 1 - \frac{1}{N} \sum_{\mathbf{x} \in X} \max_{g_i \in \mathcal{M}(\mathbf{x})} p_i(\mathbf{x})$$

This loss encourages highly confident (low-entropy) assignments, thereby reducing ambiguity and stabilizing optimization. To prevent excessive expansion of Gaussians caused by the divergence objective and ensure that each Gaussian accurately aligns with its assigned points, we introduce the anchor loss  $\mathcal{L}_{\text{anchor}}$ :

$$\mathcal{L}_{\text{anchor}} = \frac{1}{d|G|} \sum_{g_i \in G} \left( \|\mu_i - \hat{\mu}_i\|_2^2 + \alpha \|\mathbf{L}_i \mathbf{L}_i^\top - \hat{\Sigma}_i\|_F^2 \right),$$

where  $\hat{\mu}_i$  and  $\hat{\Sigma}_i = \text{Cov}(x \in B_{g_i})$  are the empirical mean and covariance of points assigned to Gaussian  $g_i$ , and  $\alpha$  is a hyperparameter balancing position and shape. This loss constrains Gaussians by anchoring them closely to their local data distributions, counteracting uncontrolled growth from other loss terms and maintaining geometric alignment and interpretability. Finally, our loss function is defined as:

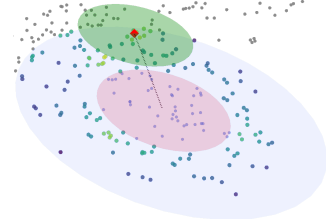
$$\mathcal{L} = \lambda_{\text{div}} \cdot \mathcal{L}_{\text{div}} + \lambda_{\text{cov}} \cdot \mathcal{L}_{\text{cov}} + \lambda_{\text{anchor}} \cdot \mathcal{L}_{\text{anchor}},$$

where  $\lambda_{\text{div}}$ ,  $\lambda_{\text{cov}}$  and  $\lambda_{\text{anchor}}$  are hyperparameters balancing the importance of each term.

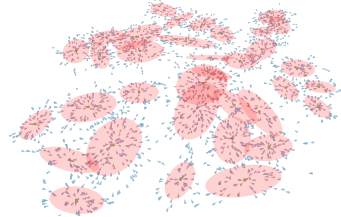
### 2.3 Adaptive Refinement

Controlling the number of Gaussians during training is key for adapting to data complexity; allocating more in dense regions and fewer in simpler ones. We employ an adaptive refinement strategy that adjusts the Gaussian set based on local point density. Prior approaches rely on positional gradients to guide refinement [29], but these become sparse and unreliable in high dimensions. In our case, we also require search efficiency, so we refine Gaussians whose bucket cardinality exceeds a threshold:  $|\mathcal{B}_g| > \gamma \cdot |X|$ . Splitting is performed by applying DBSCAN [17] to detect two dense clusters within the bucket. If unsuccessful, we fall back to K-Means to produce new means  $\mu_1, \mu_2$ , while covariances are scaled down as  $\mathbf{L}_1 = \mathbf{L}_2 = \alpha \cdot \mathbf{L}$ , with  $\alpha < 1$ .

For cloning, we target Gaussians with a high ratio of outside points to interior ones  $\mathcal{B}_{g_i}^{\text{in}} = \{\mathbf{x} \in X : \delta_M(\mathbf{x}, g_i) \leq \tau\}$ . Instead of using all nearest outside points, we focus on a boundary region, and select  $k = \rho \cdot |\mathcal{B}_g^{\text{out}}|$  points, where  $\rho \in (0, 1)$  is a sampling ratio and  $\mathcal{B}_{g_i}^{\text{out}} = \{\mathbf{x} \in X : \tau < \delta_M(\mathbf{x}, g_i) < e\tau \text{ and } g_i = \arg \min_{g_j \in G} \delta_M(\mathbf{x}, g_j)\}$  with  $e > 1$  is the set of all boundary points. The sampled subset  $S = \{\mathbf{x}_1, \mathbf{x}_2, \dots, \mathbf{x}_k\} \subset \mathcal{B}_g^{\text{out}}$  is chosen randomly without replacement. This sampling approach serves several purposes, reducing computational cost, as density estimation in high dimensions is expensive, providing statistical robustness by focusing on representative points and helping to avoid outliers that might exist in the boundary region as Fig. 2 showcases.



(a) Clone operation. (light red) region where  $d_M(x, g_i) \leq \tau$ ; (blue) outer shell  $\tau < d_M(x, g_i) \leq e\tau$ ; (gray)  $\{x : d_M(x, g_i) \geq e\tau\}$ ; (red) mean of the new gaussian; (green) new covariance matrix. (purple - lime) denote increasing data density.



(b) Grad flow:  $\mathcal{L}_{\text{div}}$ ,  $\mathcal{L}_{\text{cov}}$ ,  $\mathcal{L}_{\text{anchor}}$

Figure 2: Gaussian refinement and associated loss gradients.

The candidate Gaussians are picked with regards to the ration of boundary to interior points:  $|\mathcal{B}_g^{out}|/|\mathcal{B}_g^{in}| > \beta$ . The center of the new Gaussian is placed at the point with the highest local density in the boundary region, such that for a point  $\mathbf{p}$  in the boundary region, we compute its local density as:

$$\rho(\mathbf{p}) = \frac{1}{\frac{1}{k} \sum_{j=1}^k \delta_{\mathcal{E}}(\mathbf{p}, \text{NN}_j(\mathbf{p}))},$$

here  $\text{NN}_j(\mathbf{p})$  is the  $j$ -th nearest neighbor of  $\mathbf{p}$  and  $\delta_{\mathcal{E}}(\cdot, \cdot)$  is the Euclidean distance. We select the point with the highest density:  $\mathbf{p}^* = \arg \max_{\mathbf{p}} \rho(\mathbf{p})$ . The covariance matrix is then cloned, with  $\mathbf{L}_{new} = \mathbf{L}$ .

## 2.4 Quantization

After optimizing our Gaussians, we assign points that fall outside the coverage radius to the nearest Gaussian such that our final buckets are:

$$B_{g_i} = \{\mathbf{x} \in X \mid \delta_M(\mathbf{x}, g_i) \leq \tau\} \cup \{\mathbf{x} \in X \mid \delta_M(\mathbf{x}, g_i) > \tau \text{ and } g_i = \arg \min_{g_j \in \mathcal{G}} \delta_M(\mathbf{x}, g_j)\}$$

---

### Algorithm 1 Build Index

---

```

1: Input: Dataset  $\mathcal{D}$  of  $d$ -dimensional points
2: Initialize Gaussians on  $\mathcal{D}$ 
3:  $\mathcal{G} \leftarrow$  Obtain  $K$  Gaussians  $g_i = \mathcal{N}(\mu_i, L_i)$  (Sec. 2.2, 2.3)
4: for each point  $p$  do
5:   Assign  $p$  to all Gaussians where  $d_M(p, g_i) < \tau, \forall i \in [K]$ 
6:   if  $p$  not assigned to any Gaussian then
7:     Assign  $p$  to nearest Gaussian w.r.t.  $d_M$ 
8:   end if
9: end for
10: for each Gaussian  $g_i \in \mathcal{G}$  do
11:    $\mathcal{Q}_i \leftarrow$  Quantize indexed data of  $g_i$  (Sec. 2.4)
12: end for
13: return  $\{(g_i, \mathcal{Q}_i)\}_{i \in [K]}$ 

```

---

While our Gaussian-based buckets provide an effective organization of the data space, exhaustive search within buckets becomes prohibitively expensive as dimensionality increases. For high-dimensional nearest neighbor search, we must avoid calculating distances to all points within candidate buckets. Standard approximate search methods, however, often do not account for the unique structure provided by our Gaussian-based partitioning.

We introduce a quantization scheme that leverages the inherent properties of our Gaussian model. The key insight is that once we have assigned points to appropriate Gaussian buckets, we can apply efficient Euclidean-based quantization within each bucket's local coordinate system, reducing the number of distance computations required at

query time.

For each bucket  $B_g$ , we apply PCA to reduce dimensionality while preserving the local structure  $\mathbf{P}_g = \text{PCA}(\{\mathbf{x} - \bar{\mathbf{x}}_g \mid \mathbf{x} \in B_g\}, r)$  where  $\bar{\mathbf{x}}_g$  is the mean of points in bucket  $B_g$ ,  $r$  is the reduced dimensionality (typically  $r \ll d$ , constant in practice), and  $\mathbf{P}_g \in \mathbb{R}^{d \times r}$  contains the principal components. Each point  $\mathbf{x} \in B_g$  is projected into this lower-dimensional space  $\mathbf{x}^r = \mathbf{P}_g^T(\mathbf{x} - \bar{\mathbf{x}}_g)$ , after which its transformed to hyperspherical coordinates  $\mathbf{s} = \text{cart2sph}(\mathbf{x}^r)$ , where the transformation for an  $r$ -dimensional point yields coordinates  $\mathbf{s} = (s_1, s_2, \dots, s_r)$ .

The hyperspherical space is then partitioned into bins defined by  $n_r$  radial divisions and  $n_a$  angular divisions per dimension:  $\mathcal{B}_g = \{B_{i,\mathbf{j}} \mid i \in \{1, \dots, n_r\}, \mathbf{j} \in \{1, \dots, n_a\}^{r-1}\}$  with boundaries  $r_i = r_{\min} + (r_{\max} - r_{\min}) \cdot i/n_r$ ,  $i \in \{0, \dots, n_r\}$  and  $\theta_{j,k} = \theta_{\min,k} + (\theta_{\max,k} -$

---

### Algorithm 2 Query Index

---

```

1: Input: Index structure set  $\{(g_i, \mathcal{Q}_i)\}_{i \in [K]}$ , query  $q$ 
2:  $g_i \leftarrow \arg \min_{i: g_i \in \mathcal{G}} d_M(q, g_i)$ 
3:  $B \leftarrow$  Traverse subset of bins from  $\mathcal{Q}_i$  (Sec. 2.4)
4: Measure  $L_2$  distance to candidates in  $B$ 
5: Terminate if condition (Sec. 2.5)
6: return nearest neighbor of  $q$  in  $B$ 

```

---

$\theta_{\min,k}) \cdot j/n_a$ ,  $j \in \{0, \dots, n_a\}$ ,  $k \in \{1, \dots, r-1\}$ . Alg. 1 illustrates the construction process of the index structure.

## 2.5 Inference

At query time, for a query point  $\mathbf{q}$ , we employ a multi-stage approach to efficiently retrieve approximate nearest neighbors. First, we identify the  $k$  nearest Gaussians using the Mahalanobis distance. For each selected Gaussian bucket  $g$ , we project the query into the bucket’s local PCA space,  $\mathbf{q}_g^r = \mathbf{P}_g^T(\mathbf{q} - \bar{\mathbf{x}}_g)$ , and convert it to hyperspherical coordinates  $\mathbf{s}_g = \text{cart2sph}(\mathbf{q}_g^r)$ . We then compute the distances to all bins in the bucket and sort them in ascending order. For each bin  $B_{i,j}$  with boundaries defined by  $r$ -intervals  $[r_i, r_{i+1}]$  and angular intervals  $[\theta_{j,k}, \theta_{j+1,k}]$ , we compute the distance  $d(\mathbf{s}_g, B_{i,j}) = \min_{\mathbf{y} \in B_{i,j}} \|\mathbf{s}_g - \mathbf{y}\|_2$ .

This minimization problem is efficiently solved by first checking if  $\mathbf{s}_g$  is inside the bin. If it is outside, we solve the constrained optimization problem by initializing a point  $\mathbf{y}^0$  with its radial component clipped to  $[r_{\min}, r_{\max}]$  and angular components set to the midpoints of their respective intervals. We then minimize  $\|\mathbf{s}_g - \mathbf{y}\|_2$  subject to the bin boundary constraints using the L-BFGS-B [10] algorithm, which respects the bounds  $r_{\min} \leq y_1 \leq r_{\max}$  and  $\theta_{\min,j} \leq y_{j+1} \leq \theta_{\max,j}$  for the radial and angular components respectively.

We then search for points in bins sequentially according to their sorted distances, computing exact Euclidean distances between the query and the points in each bin. The search terminates under the condition that we have examined a predefined percentage of bins (typically 30%). Given a query, Alg. 2 showcases the procedure of retrieving the nearest neighbor using our index structure.

## 3 Experiments

**Datasets.** We evaluate our method on three benchmark datasets: SIFT1M [37] (128-dimensional image descriptors with one million points), MNIST [32] and Fashion-MNIST [44] (784-dimensional vectors from  $28 \times 28$  grayscale images). These datasets provide diverse characteristics in terms of extrinsic and intrinsic dimensionality, scale, and data distribution, offering a comprehensive evaluation framework in Euclidean space. Additional information about the datasets and their licenses are provided in the Supplementary Material (SM).

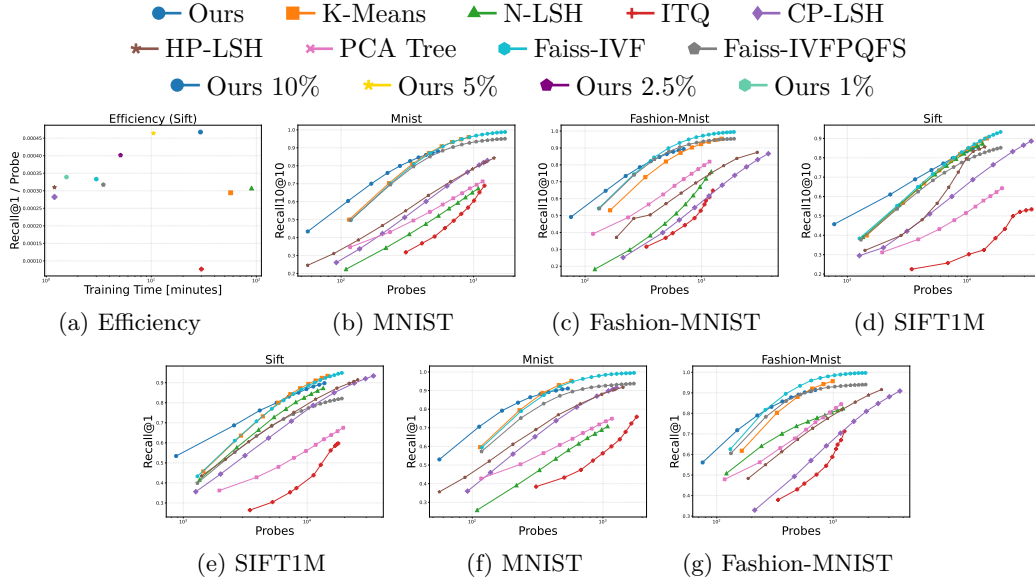


Figure 3: Efficiency and retrieval performance across datasets, measured via Recall@1 and Recall10@10. Methods closer to the top-left ( $\nwarrow$ ) indicate a better trade-off between accuracy and candidate count. Our method performs especially well in the low-probe regime.

**Evaluation.** We evaluate our method on retrieval and classification tasks across the aforementioned datasets. For retrieval, we report Recall10@10 and Recall@1 versus the number of retrieved candidates (probes), reflecting the trade-off between accuracy and efficiency. Recall10@10 measures how many of the true top-10 neighbors are in the retrieved set, while Recall@1 checks if the top-ranked result is the true nearest neighbor. The candidate count controls query time and serves as the main efficiency metric. For MNIST and Fashion-MNIST, we assess classification via majority voting over retrieved candidates:  $\hat{y}(q) = \arg \max_c \sum_{x \in C_q} \mathbb{I}[\text{label}(x) = c]$ . This evaluates how well the partitioning preserves semantic similarity.

**Baselines and Comparisons.** We evaluate our proposed method against several state-of-the-art approximate nearest neighbor search algorithms such as K-Means [6], Neural-LSH (N-LSH) [14], Hyperplane LSH (HP-LSH) [25, 5], Cross-polytope LSH (CP-LSH) [5], ITQ [19], PCA Tree [31, 1, 41, 39], and Faiss-IVF and Faiss-IVFPQFS [15]. For classification tasks, we additionally compare against standard  $k$ -Nearest Neighbors ( $k$ -NN) [12, 42], which performs exhaustive search for exact neighbors, and  $k$ -K-Nearest Neighbors ( $k$ K-NN) [33], which adjusts the neighborhood size based on local curvature estimates. Each method was evaluated under identical conditions, with hyperparameters optimized according to their original publications to ensure fair and meaningful comparisons across both nearest neighbor retrieval and classification performance.

**Results and Analysis.** We present performance curves across datasets, reporting Recall10@10 and Recall@1 as a function of the number of retrieved candidates. As shown in Fig. 3, our method consistently outperforms state-of-the-art baselines across both metrics. Notably, it exhibits a significant advantage in the low-probe regime: for example, on SIFT1M, our method achieves Recall@1 of  $\sim 69\%$  using  $\sim 3400$  candidates, compared to 61% for Faiss-IVF and 55% for Faiss-IVFPQFS using similar candidate counts. This efficiency gap is most evident below the 80% recall threshold, where traditional methods struggle to match the accuracy without a sharp rise in probe cost. Fig. 3(a) highlights the efficiency trade-off between training time and retrieval quality, measured via Recall@1-per-probe. All our variants lie in the top-left region of the plot, offering options ranging from ultra-fast lightweight models (e.g., Ours 1%) to more accurate, higher-capacity variants (e.g., Ours 10%). In contrast, competing methods tend to occupy lower-efficiency or higher-cost zones, demonstrating a less favorable balance between indexing overhead and retrieval quality.

Table 1: Classification accuracy via majority voting. Ours-1:  $\arg \min_g \delta_M(q, g)$ ; Ours-2:  $\delta_M(q, g) \leq \tau$ ; Ours-3: top- $k$  Gaussians. We highlight the **best**, **second-best** and **third-best** results.

Method	Dataset	
	MNIST $\uparrow$	Fashion-MNIST $\uparrow$
k-NN	0.7576	0.7133
kK-NN	0.7609	0.7796
K-Means	0.9118	0.7589
PCA Tree	0.7750	0.7427
ITQ	0.7156	0.6459
HP-LSH	0.5483	0.6643
CP-LSH	0.7801	0.7128
N-LSH	0.4142	0.4307
Faiss-IVF	0.9180	0.8070
Faiss-IVFPQFS	0.9210	0.7930
Ours-1	0.9332	0.8020
Ours-2	0.9330	0.8156
Ours-3	0.9175	0.7879

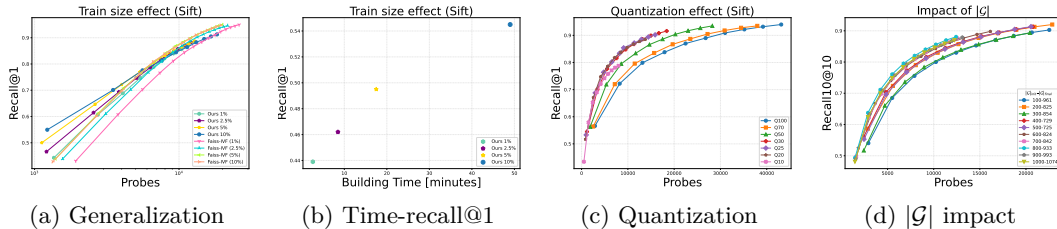


Figure 4: (a) Generalization with limited training data. (b) Time-recall@1 tradeoff. (c) Quantization: efficient search via partial bucket scanning. (d) Impact of initial number of Gaussians.



Furthermore, for classification tasks on MNIST and Fashion-MNIST, our approach demonstrates superior classification accuracy compared to the other benchmarks, shown in Tab.1. This enhancement is consistent with theoretical expectations, as our methodology learns the inherent probabilistic structure of the training data rather than depending on predetermined heuristics, static partitioning, or hash-based approximations. By dynamically adapting to the statistical properties of the data distribution, our method identifies more semantically coherent neighbors. Our results suggest that GARLIC acts as a local manifold modeler, not just an indexing method offering smoother, distribution-aware retrieval and classification.

**Ablation study.** We investigate the robustness and data efficiency of our method through controlled down-sampling of the training set. As shown in Fig. 4(a), our method consistently maintains strong performance across varying training sizes. Notably, even with only 1% of the training data, our model outperforms the Faiss-IVF variants of up to 10% training size in terms of Recall@1 versus the number of retrieved candidates. This trend remains consistent across higher percentages, demonstrating that our approach learns a compact yet highly effective representation of the data distribution. Furthermore, Fig. 4(b) highlights the favorable scaling of our method with respect to training time, while Fig. 4(c) demonstrates the impact of our quantization scheme. In particular, it exhibits strong performance across a broad quantization range (20 – 100%), with only the most aggressive setting (10%) leading to degradation. This indicates that our quantization strategy is robust and well-aligned with our model structure. Fig. 4(c) shows that increasing the number of initial Gaussians accelerates convergence. However, the primary role of adaptive refinement is not to fix the final count, but to control their spatial density.

Table 2: Effect of loss terms and adaptive refinement on average Recall10@10 / Probe ( $\times 10^5$ ). Higher is better.

Configuration	Performance $\uparrow$
Loss terms	
w/ all	10.43
$\mathcal{L}_{div} + \mathcal{L}_{cov}$	9.82
$\mathcal{L}_{div} + \mathcal{L}_{anchor}$	7.87
$\mathcal{L}_{div}$	7.17
Split & Clone	
w/ both	10.43
w/ split	8.65
w/ clone	8.47
w/o any	2.79

Tab. 2 analyzes the impact of loss terms and adaptive refinement. Split and clone are pivotal for performance, while the covariance term ( $\mathcal{L}_{cov}$ ) significantly boosts retrieval. The anchor term ( $\mathcal{L}_{anchor}$ ) has minor effect on raw performance but is essential for making Gaussians geometrically informative. Additional ablations and results, covering hyperparameter sensitivity, design variants, and the ability of Gaussians to capture non-linear, informative structure, are provided in the SM.

**Limitations.** GARLIC uses Mahalanobis distance, which assumes Euclidean structure and is not directly compatible with angular similarity. This can be addressed by replacing Gaussians with angular analogues such as von Mises–Fisher distributions or by embedding into hyperspherical spaces. Although GARLIC performs strongly in low-probe regimes, achieving very high recall (e.g.,  $\geq 95\%$ ) requires more computation. This recall-latency trade-off can be mitigated by increasing the number of Gaussians and structuring them with trees (e.g., KD-tree or Ball-tree over Gaussian means), reducing query cost. The space complexity scales quadratically with the dimension ( $O(Kd^2)$ ) due to full anisotropic covariances; however, this can be alleviated by using diagonal or low-rank approximations, or by quantizing the Cholesky factors. Lastly, while the method is mildly sensitive to initialization, its impact is reduced by the information-theoretic objectives and the progressive refinement through split and clone operations.

## 4 Conclusions

We introduced GARLIC, a geometric structure that learns the underlying distribution for both approximate nearest neighbor search and classification. By combining information-theoretic objectives with adaptive refinement (split and clone), and representing the space via anisotropic Gaussians with local quantization, our method achieves strong performance in both retrieval and classification, particularly in low-probe regimes. Experiments demonstrate competitive recall-efficiency tradeoffs and robustness under severe data reduction, highlighting its generalization capabilities.

## Acknowledgments

PR and IE were partially supported by project MIS 5154714 of the National Recovery and Resilience Plan Greece 2.0 funded by the European Union under the NextGenerationEU Program. PR, CT, IC, GI and IE have been partially supported by the European Union and the “Greece 2.0” national recovery and resilience plan, under the call "RESEARCH-CREATE-INNOVATE" (Code: TAEΔK-06168).

## References

- [1] Amirali Abdullah, Alexandr Andoni, Ravindran Kannan, and Robert Krauthgamer. Spectral approaches to nearest neighbor search. In 2014 IEEE 55th Annual Symposium on Foundations of Computer Science, pages 581–590. IEEE, 2014.
- [2] Charu C Aggarwal, Alexander Hinneburg, and Daniel A Keim. On the surprising behavior of distance metrics in high dimensional space. In International conference on database theory, pages 420–434. Springer, 2001.
- [3] Liefu Ai, Junqing Yu, Zebin Wu, Yunfeng He, and Tao Guan. Optimized residual vector quantization for efficient approximate nearest neighbor search. Multimedia Systems, 23: 169–181, 2017.
- [4] Evangelos Anagnostopoulos, Ioannis Z Emiris, and Ioannis Psarros. Randomized embeddings with slack and high-dimensional approximate nearest neighbor. ACM Transactions on Algorithms (TALG), 14(2):1–21, 2018.
- [5] Alexandr Andoni, Piotr Indyk, Thijs Laarhoven, Ilya Razenshteyn, and Ludwig Schmidt. Practical and optimal lsh for angular distance. In C. Cortes, N. Lawrence, D. Lee, M. Sugiyama, and R. Garnett, editors, Advances in Neural Information Processing Systems, volume 28. Curran Associates, Inc., 2015. URL [https://proceedings.neurips.cc/paper\\_files/paper/2015/file/2823f4797102ce1a1aec05359cc16dd9-Paper.pdf](https://proceedings.neurips.cc/paper_files/paper/2015/file/2823f4797102ce1a1aec05359cc16dd9-Paper.pdf).
- [6] David Arthur and Sergei Vassilvitskii. k-means++: The advantages of careful seeding. Technical report, Stanford, 2006.
- [7] David Arthur and Sergei Vassilvitskii. k-means++: the advantages of careful seeding. In Proceedings of the Eighteenth Annual ACM-SIAM Symposium on Discrete Algorithms, SODA '07, page 1027–1035, USA, 2007. Society for Industrial and Applied Mathematics. ISBN 9780898716245.
- [8] Martin Aumüller, Erik Bernhardsson, and Alexander Faithfull. Ann-benchmarks: A benchmarking tool for approximate nearest neighbor algorithms. Information Systems, 87:101374, 2020.
- [9] Adrien Bardes, Jean Ponce, and Yann LeCun. VICReg: Variance-invariance-covariance regularization for self-supervised learning. In International Conference on Learning Representations, 2022. URL <https://openreview.net/forum?id=xm6YD62D1Ub>.
- [10] Richard H Byrd, Peihuang Lu, Jorge Nocedal, and Ciyou Zhu. A limited memory algorithm for bound constrained optimization. SIAM Journal on scientific computing, 16(5):1190–1208, 1995.
- [11] Chih-Yi Chiu, Amorntip Prayoonwong, and Yin-Chih Liao. Learning to index for nearest neighbor search. IEEE Transactions on Pattern Analysis and Machine Intelligence, 42(8):1942–1956, 2020. doi: 10.1109/TPAMI.2019.2907086.
- [12] Thomas Cover and Peter Hart. Nearest neighbor pattern classification. IEEE transactions on information theory, 13(1):21–27, 1967.
- [13] Thanh-Toan Do, Anh-Dzung Doan, and Ngai-Man Cheung. Learning to hash with binary deep neural network. In Computer Vision–ECCV 2016: 14th European Conference, Amsterdam, The Netherlands, October 11–14, 2016, Proceedings, Part V 14, pages 219–234. Springer, 2016.

- [14] Yihe Dong, Piotr Indyk, Ilya Razenshteyn, and Tal Wagner. Learning space partitions for nearest neighbor search. In International Conference on Learning Representations, 2020. URL <https://openreview.net/forum?id=rkenmREFDr>.
- [15] Matthijs Douze, Alexandr Guzhva, Chengqi Deng, Jeff Johnson, Gergely Szilvasy, Pierre-Emmanuel Mazaré, Maria Lomeli, Lucas Hosseini, and Hervé Jégou. The faiss library. arXiv preprint arXiv:2401.08281, 2024.
- [16] Venice Erin Liong, Jiwen Lu, Gang Wang, Pierre Moulin, and Jie Zhou. Deep hashing for compact binary codes learning. In Proceedings of the IEEE conference on computer vision and pattern recognition, pages 2475–2483, 2015.
- [17] Martin Ester, Hans-Peter Kriegel, Jörg Sander, Xiaowei Xu, et al. A density-based algorithm for discovering clusters in large spatial databases with noise. In kdd, volume 96, pages 226–231, 1996.
- [18] Cong Fu, Chao Xiang, Changxu Wang, and Deng Cai. Fast approximate nearest neighbor search with the navigating spreading-out graph. arXiv preprint arXiv:1707.00143, 2017.
- [19] Yunchao Gong, Svetlana Lazebnik, Albert Gordo, and Florent Perronnin. Iterative quantization: A procrustean approach to learning binary codes for large-scale image retrieval. IEEE transactions on pattern analysis and machine intelligence, 35(12):2916–2929, 2012.
- [20] Robert M. Gray and David L. Neuhoff. Quantization. IEEE transactions on information theory, 44(6):2325–2383, 1998.
- [21] Gaurav Gupta, Tharun Medini, Anshumali Shrivastava, and Alexander J. Smola. Bliss: A billion scale index using iterative re-partitioning. In Proceedings of the 28th ACM SIGKDD Conference on Knowledge Discovery and Data Mining, KDD ’22, page 486–495, New York, NY, USA, 2022. Association for Computing Machinery. ISBN 9781450393850. doi: 10.1145/3534678.3539414. URL <https://doi.org/10.1145/3534678.3539414>.
- [22] Charles R Harris, K Jarrod Millman, Stéfan J Van Der Walt, Ralf Gommers, Pauli Virtanen, David Cournapeau, Eric Wieser, Julian Taylor, Sebastian Berg, Nathaniel J Smith, et al. Array programming with numpy. Nature, 585(7825):357–362, 2020.
- [23] Geoffrey Hinton, Oriol Vinyals, and Jeff Dean. Distilling the knowledge in a neural network. arXiv preprint arXiv:1503.02531, 2015.
- [24] Ville Hyvönen, Elias Jääsaari, and Teemu Roos. A multilabel classification framework for approximate nearest neighbor search, 2022. URL <https://arxiv.org/abs/1910.08322>.
- [25] Piotr Indyk and Rajeev Motwani. Approximate nearest neighbors: towards removing the curse of dimensionality. In Proceedings of the Thirtieth Annual ACM Symposium on Theory of Computing, STOC ’98, page 604–613, New York, NY, USA, 1998. Association for Computing Machinery. ISBN 0897919629. doi: 10.1145/276698.276876. URL <https://doi.org/10.1145/276698.276876>.
- [26] Herve Jegou, Matthijs Douze, and Cordelia Schmid. Product quantization for nearest neighbor search. IEEE transactions on pattern analysis and machine intelligence, 33(1):117–128, 2010.
- [27] Qing-Yuan Jiang and Wu-Jun Li. Asymmetric deep supervised hashing. In Proceedings of the AAAI conference on artificial intelligence, volume 32, 2018.
- [28] Omid Keivani and Kaushik Sinha. Improved nearest neighbor search using auxiliary information and priority functions. In International Conference on Machine Learning, pages 2573–2581. PMLR, 2018.

- [29] Bernhard Kerbl, Georgios Kopanas, Thomas Leimkühler, and George Drettakis. 3d gaussian splatting for real-time radiance field rendering. ACM Trans. Graph., 42(4): 139–1, 2023.
- [30] Bernhard Kerbl, Georgios Kopanas, Thomas Leimkühler, and George Drettakis. 3d gaussian splatting for real-time radiance field rendering. ACM Transactions on Graphics, 42(4), July 2023. URL <https://repo-sam.inria.fr/fungraph/3d-gaussian-splatting/>.
- [31] Neeraj Kumar, Li Zhang, and Shree Nayar. What is a good nearest neighbors algorithm for finding similar patches in images? In Computer Vision–ECCV 2008: 10th European Conference on Computer Vision, Marseille, France, October 12–18, 2008, Proceedings, Part II 10, pages 364–378. Springer, 2008.
- [32] Yann LeCun, Léon Bottou, Yoshua Bengio, and Patrick Haffner. Gradient-based learning applied to document recognition. Proceedings of the IEEE, 86(11):2278–2324, 1998.
- [33] Alexandre Luís Magalhães Levada, Frank Nielsen, and Michel Ferreira Cardia Haddad. A new geometric approach of adaptive neighborhood selection for classification. In NeurIPS 2024 Workshop on Symmetry and Geometry in Neural Representations, 2024.
- [34] Zechao Li, Jinhui Tang, Liyan Zhang, and Jian Yang. Weakly-supervised semantic guided hashing for social image retrieval. International Journal of Computer Vision, 128:2265–2278, 2020.
- [35] Haomiao Liu, Ruiping Wang, Shiguang Shan, and Xilin Chen. Deep supervised hashing for fast image retrieval. In Proceedings of the IEEE conference on computer vision and pattern recognition, pages 2064–2072, 2016.
- [36] Yu Liu, Jingkuan Song, Ke Zhou, Lingyu Yan, Li Liu, Fuhao Zou, and Ling Shao. Deep self-taught hashing for image retrieval. IEEE transactions on cybernetics, 49(6): 2229–2241, 2018.
- [37] David G Lowe. Distinctive image features from scale-invariant keypoints. International journal of computer vision, 60:91–110, 2004.
- [38] Yu A Malkov and Dmitry A Yashunin. Efficient and robust approximate nearest neighbor search using hierarchical navigable small world graphs. IEEE transactions on pattern analysis and machine intelligence, 42(4):824–836, 2018.
- [39] James McNames. A fast nearest-neighbor algorithm based on a principal axis search tree. IEEE Transactions on pattern analysis and machine intelligence, 23(9):964–976, 2001.
- [40] A Paszke. Pytorch: An imperative style, high-performance deep learning library. arXiv preprint arXiv:1912.01703, 2019.
- [41] Robert F Sproull. Refinements to nearest-neighbor searching in k-dimensional trees. Algorithmica, 6:579–589, 1991.
- [42] Kashvi Taunk, Sanjukta De, Srishti Verma, and Aleena Swetapadma. A brief review of nearest neighbor algorithm for learning and classification. In 2019 international conference on intelligent computing and control systems (ICCS), pages 1255–1260. IEEE, 2019.
- [43] Dayan Wu, Qi Dai, Jing Liu, Bo Li, and Weiping Wang. Deep incremental hashing network for efficient image retrieval. In Proceedings of the IEEE/CVF conference on computer vision and pattern recognition, pages 9069–9077, 2019.
- [44] Han Xiao, Kashif Rasul, and Roland Vollgraf. Fashion-mnist: a novel image dataset for benchmarking machine learning algorithms. arXiv preprint arXiv:1708.07747, 2017.
- [45] Jure Zbontar, Li Jing, Ishan Misra, Yann LeCun, and Stéphane Deny. Barlow twins: Self-supervised learning via redundancy reduction. In International conference on machine learning, pages 12310–12320. PMLR, 2021.

- [46] Xiaofeng Zhu, Xuelong Li, Shichao Zhang, Zongben Xu, Litao Yu, and Can Wang. Graph pca hashing for similarity search. IEEE Transactions on Multimedia, 19(9): 2033–2044, 2017.

## A Supplementary Material

This supplementary material provides additional details and experiments as mentioned in the main paper. Sec. A.1 discusses and provides detailed computational time and space complexity for the build and query procedures of our proposed method. Sec. A.2 contains additional technical details regarding the datasets used and the experimental setup, as well as the training pipeline. Sec. A.3 provides ablation studies to validate our choices regarding the tuned hyperparameters of our method and the components of it (discussed in Sec.4 of the main paper). Sec. A.4 contains visualization of diagnostics and statistics regarding our proposed method, in order to provide a comprehensive understanding of its behavior.

### A.1 Complexity Analysis

We analyze the computational time and space complexity of our method in three parts: index construction, query execution, and storage. The analysis is expressed in terms of standard parameters, including the dataset size  $|X|$ , embedding dimension  $d$ , the number of Gaussians  $K$ , and the reduced PCA dimension  $r \ll d$ . Our goal is to ensure that each component remains scalable with respect to high-dimensional data and large-scale datasets. We summarize the complexity of each phase below.

**Index build complexity.** Let  $|X|$  be the number of data points,  $d$  the embedding dimension,  $K'$  the initial number of Gaussians, and  $r \ll d$  the reduced dimension used for local quantization. Let  $I$  be the number of optimization steps. We denote by  $S$ ,  $C$ , and  $P$  the number of splits, clones, and pruned Gaussians, respectively, and define the final number of Gaussians as  $K = K' + S + C - P$ . Let  $|B_g|$  be the average bucket size,  $c$  the number of K-Means clusters used during splitting, and  $k'$  the number of candidate points sampled per clone.

For the initialization, since we use K-Means++ on  $K'$  total cluster centers, we need  $\mathcal{O}(K' \cdot d \cdot |X|)$  time. For the optimization part, we need to perform a total number of  $I$  iterations of full Mahalanobis-based point-to-Gaussian assignment, thus a total of  $\mathcal{O}(I \cdot |X| \cdot K \cdot d^2)$  worst-case time. Separate from the optimization, we analyze the split, clone and prune operations that are not applied on every iteration of the optimization. (i) The split operation runs DBSCAN or K-Means (with  $c$  clusters), thus for a total of  $S$  such operations we would need  $\mathcal{O}(S \cdot (|B_g| \cdot d \cdot c + d^2))$ ; (ii) the clone operation locates the subset of points outside the Gaussian's boundary (e.g., between  $\tau \cdot \sigma$  and  $(1 + \epsilon) \cdot \tau \cdot \sigma$ ) for which it identifies new local modes, thus for a total of  $C$  operations, it leads to  $\mathcal{O}(C \cdot (k'^2 \cdot d + d^2))$ ; and (iii) the prune operation simply removes low-cardinality Gaussians and reassigns the points to the nearest active Gaussian, which takes  $\mathcal{O}(P \cdot |B_g| \cdot d)$  time. For the quantization of each Gaussian, PCA is performed on all points inside the Gaussian, which projects the data into reduced local bases. In total, for the quantization we need  $\mathcal{O}(K' \cdot |B_g| \cdot d^2 + |X| \cdot d \cdot r)$  time.

**Query complexity.** Let  $K$  be the number of Gaussians,  $k$  the number selected per query,  $d$  the dimension,  $r$  the PCA dimension,  $b$  the number of bins per Gaussian,  $T$  the number of optimization steps to find the shortest distance from the query point to the boundary of a spherical bin in the reduced PCA space,  $\rho$  the probed bin ratio, and  $\beta$  the average bin size. For a single query, we first need to measure distances from the set of Gaussians, which takes  $\mathcal{O}(K \cdot d^2)$ . Then, for the  $k$  nearest Gaussians we need to locate the subset of data to be examined. For this, for each of the selected  $k$  Gaussians, we need to compute the local PCA projections ( $\mathcal{O}(k \cdot d \cdot r)$ ), then compute and sort the spherical distances to all  $b$  bins ( $\mathcal{O}(k \cdot b \cdot r \cdot T)$ ), of which only the  $\rho$  fraction is probed. From each, up to  $\beta$  candidates are gathered and re-ranked using Euclidean distance, which needs  $\mathcal{O}(k \cdot \rho \cdot b \cdot \beta \cdot d)$  time. In practice, the re-ranking factor dominates the complexity, which is sublinear.

**Space complexity.** Let  $K$  be the number of Gaussians,  $d$  the data dimension, and  $N = |X|$  the dataset size. The model stores mean vectors  $\boldsymbol{\mu} \in \mathbb{R}^{K \times d}$ , Cholesky parameters  $\mathbf{L} \in \mathbb{R}^{K \times d \times d}$ , and Buckets storing point indices, requiring  $\mathcal{O}(N)$  space. Thus, the total space complexity is:

$$\mathcal{O}(K \cdot (d^2 + d) + N)$$

where  $K \cdot d^2$  dominates. Still, space complexity can be reduced to  $\mathcal{O}(K \cdot d)$  by enforcing diagonal covariance matrices, at the expense of reduced expressiveness in anisotropic regions of the space.

## A.2 Implementation details

This subsection summarizes all implementation and training-specific parameters used in our model, including optimizer schedules, architectural constants, and adaptive procedures such as splitting, cloning and pruning. These details provide context for reproducibility and support the complexity analysis in the main paper. Furthermore, there are dataset specifics, such as licenses and descriptions.

Table 3: Dataset Information

Dataset	Dimension	Size	Description	License
SIFT1M	128	1M	Image descriptors	CC0
MNIST	784	70K	Handwritten digits	CC BY-SA 3.0
Fashion-MNIST	784	70K	Fashion items	MIT

**Datasets.** We evaluate our method on three standard benchmark datasets: (1) SIFT1M [37], containing one million 128-dimensional SIFT descriptors that capture scale- and rotation-invariant local image features; (2) MNIST [32], consisting of 70,000 grayscale handwritten digit images (28×28 pixels) flattened to 784-dimensional vectors; and (3) Fashion-MNIST [44], a more challenging variant with the same format but featuring 10 categories of fashion items. For retrieval tasks, we used the ANN-Benchmark [8] versions of these datasets (available at <http://ann-benchmarks.com/sift-128-euclidean.hdf5>, <http://ann-benchmarks.com/mnist-784-euclidean.hdf5>, and <http://ann-benchmarks.com/fashion-mnist-784-euclidean.hdf5>) to ensure a standardized comparison with existing methods. For MNIST and Fashion-MNIST classification experiments, we utilized the PyTorch torchvision implementations to maintain consistency with established classification benchmarks.

**Experimental setup.** Our method was implemented in Python, using optimized libraries such as PyTorch [40] and NumPy [22]. The experiments were carried out on an Intel Core i7-7820X CPU (16 threads), a Quadro RTX 8000 GPU (48 GB VRAM) and 125 GiB of RAM.

**Training configuration.** Batch sizes of 20000 are used for SIFT, and 5000 for MNIST and Fashion-MNIST datasets, with normalization by subtracting the mean and dividing by the standard deviation. The number of training epochs is 250, with a typical early stop at 120. Gaussian updates are scheduled with two phases: a warm-up phase lasting 35 epochs and an optimization phase where structural operations like splitting and cloning are triggered every 35 epochs and pruning every 60.

**Learning rate schedule.** The learning rates follow a linear warm-up and exponential decay scheme. Specifically, for the Cholesky parameters, the rates are subjected to a warm-up phase from  $1 \times 10^{-7}$  to  $5 \times 10^{-4}$ , followed by a decay to  $9 \times 10^{-5}$ . In terms of the means, they are warmed up from  $1 \times 10^{-7}$  to  $9 \times 10^{-3}$ , and subsequently decay to  $3 \times 10^{-3}$ . Notably, the learning rate associated with the means is maintained at a relatively higher level than that of the covariances. This approach is designed to promote the adjustment of the Gaussian centers rather than the expansion of their radii.

**Adaptive refinement.** Splitting is applied to Gaussians with cardinality exceeding a fraction of the dataset  $\gamma = 1 \times 10^{-2}$ , using DBSCAN or K-Means, as fallback, with  $c = 2$  clusters. The covariance of each new Gaussian is scaled down by  $9 \times 10^{-1}$ . Cloning selects dense regions just outside the Gaussian boundary, defined by a Mahalanobis shell with inner threshold  $\tau$  and outer threshold  $(1 + \epsilon) \cdot \tau$ , where  $\epsilon = 2.2$  controls the shell thickness. From

the set of points referenced in  $(\tau, e\tau]$ , a random selection of 60% is made. Cloning is not performed on a Gaussian unless its cardinality surpasses a threshold specified by  $8 \times 10^{-4}|X|$ . Gaussians that have degenerated into a single point are eliminated. Pruning is executed at intervals of every 60 epochs.

**Quantization.** Local PCA is performed per bucket using top-3 eigenvectors. Reduced points are quantized using a spherical grid with  $n_{\text{radial}} = 6$  and  $n_{\text{angular}} = 4$ , forming directional bins per Gaussian.

**Loss.** The total loss is a weighted sum of three components: divergence  $\lambda_{\text{div}} = 1.0$ , covariance  $\lambda_{\text{cov}} = 1.0$ , and anchor term  $\lambda_{\text{anchor}} = 10^{-2}$ , with a weight  $\alpha = 10^{-1}$  that balances position and shape. When calculating the  $\mathcal{L}_{\text{cov}}$  loss, a numerical epsilon of  $1 \times 10^{-12}$  is used to ensure stability.

### A.3 Additional Ablation Studies

We extend the analysis of the experimenta section, by further examining the impact of individual design choices in GARLIC. Unless noted otherwise, for each result presented, we sample a training set of 50.000 (5%) from SIFT-1M and only change the requested parameters while keeping all others as is. In each figure, the parameters used in the main experiments are represented by the method indicated by the blue dashed line, and optimal outcomes are achieved when positioned on the top left of the figures ( $\nwarrow$ ).

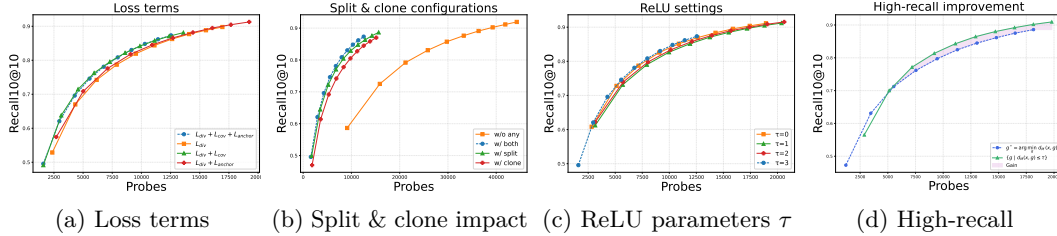


Figure 5: Parameter ablations: (a) Impact of different loss term combinations on the Recall-Probe tradeoff, showing that the full loss ( $L_{\text{div}} + L_{\text{cov}} + L_{\text{anchor}}$ ) provides the best balance. (b) Effect of split and clone operations, demonstrating that these operations improve efficiency while maintaining accuracy. (c) Impact of ReLU parameter  $\tau$  in the divergence loss. (d) Improving high-recall scenarios using all  $g$  s.t.  $d_M(x, g) \leq \tau$ . The blue dashed method regards the parameters used in main experiments, and top-left is better ( $\nwarrow$ ).

**Architectural components.** In Fig. 5(a), the contribution of each loss term to the optimization process is analyzed. The results indicate that the covariance loss  $\mathcal{L}_{\text{cov}}$  produces the most significant performance improvement, while the anchor loss  $\mathcal{L}_{\text{anchor}}$  functions as an effective regularizer, grounding each Gaussian by aligning it with its corresponding point distribution. Fig. 5(b) demonstrates the effects of our adaptive refinement operations, where the split and clone mechanisms improve retrieval performance when used together, each contributing by providing complementary benefits to the quality of representation. Fig. 5(c), addresses the parameter  $\tau$  within  $\mathcal{L}_{\text{div}}$ , demonstrating that  $\tau = 3$  is the optimal choice, particularly in scenarios involving a limited number of probes. Values surpassing those presented in our study ( $\tau > 3$ ) result in less optimal outcomes. For instance,  $\tau = 4$  demonstrates a Recall10@10 value of 0.67 when evaluated with 65000 probes.

A way to address the limitation associated with high-recall scenarios, as discussed in the limitations paragraph of the main paper, is show in Fig. 5(d). Specifically, it involves assessing all Gaussian candidates that meet the condition  $d_M(x, g) \leq \tau$ , rather than solely the one that minimizes the Mahalanobis distance. This approach is also semantically justified, considering that multiple Gaussians may occupy the same region. Consequently, a hybrid approach can be used, utilizing the argmin strategy for scenarios with a low number of probes and employing all candidates that satisfy condition  $d_M(x, g) \leq \tau$  for high-recall cases, thus effectively addressing the limitation.



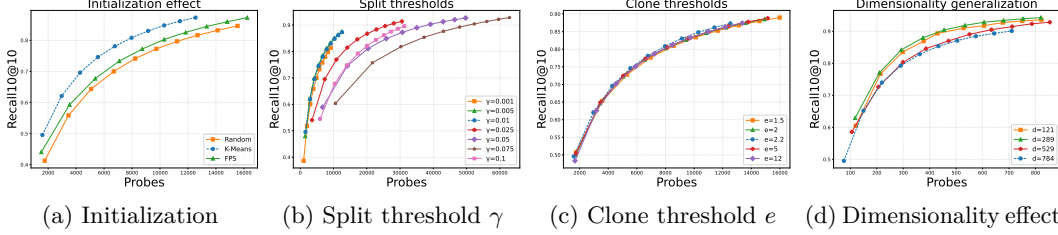


Figure 6: Hyperparameter ablations: (a) Effect of different initialization strategies. (b) Impact of split threshold  $\gamma$ , with higher values increasing accuracy at the cost of more probes. (c) Effect of clone threshold  $e$ , with  $e = 2.2$  providing the best efficiency. (d) Effect of embedding dimensionality, showing GARLIC’s robustness across different dimensions. The blue dashed method regards the parameters used in main experiments, and top-left is better ( $\nearrow$ ).

**Validation of hyperparameters.** Fig. 6 provides a systematic evaluation of our key hyperparameters. In Fig. 6(a), we investigate initialization strategies for Gaussian centers, revealing that K-Means initialization consistently outperforms alternatives. Although farthest point sampling (FPS) achieves comparable recall, it requires approximately 50% more probes, and catching up to K-Means requires more training time. In Fig. 6(b), the split threshold  $\gamma$ , controlling the density condition for Gaussian subdivision, is examined. The optimal values are  $\gamma = 0.005$  and  $\gamma = 0.01$ , though  $\gamma = 0.005$  requires more time due to more frequent splits. As for the clone threshold  $e$ , depicted in Fig. 6(c), which determines the outer shell for cloning, it remains stable across different values, with  $e = 2.2$  being preferable in situations requiring high recall. Finally, Fig. 6(d) examines dimensionality effects using Fashion-MNIST data resized to various dimensions. The results confirm that GARLIC maintains strong performance across a wide range of dimensionalities, highlighting its robustness to the feature space complexity.

Table 4: Effect of anisotropy on average Recall10@10 / Probe ( $\times 10^5$ ). Higher is better. As anisotropy decreases, performance degrades due to excessive probe usage.

Configuration	Performance $\uparrow$
Covariance structure	
Anisotropic	10.43
Diagonal	1.04
Isotropic	0.63

**Covariance structure vs performance.** We conduct a targeted study to assess the impact of different covariance configurations—namely, full (anisotropic), diagonal, and isotropic—on the performance of GARLIC. As shown in Table 4, reducing the Gaussian expressiveness from full to diagonal and then to isotropic leads to a notable decline in average Recall10@10 per probe. While diagonal and isotropic configurations reduce both the parameter count and computation per Gaussian to a linear level,  $\mathcal{O}(k \cdot d)$ , they lead to aggressive pruning and an increased number of probes to make up for the representational loss. This suggests that space complexity cannot be drastically reduced without harming retrieval quality because simpler Gaussian parameterizations result in degraded locality and coverage.

#### A.4 Qualitative Results

To gain a more comprehensive understanding of the model’s behavior, we present a collection of diagnostic visualizations applied to the Fashion-MNIST, MNIST, and SIFT datasets. These plots illustrate structural characteristics, including local coverage, reconstruction fidelity, density patterns, and curvature statistics of the learned Gaussian components. All visualizations are conducted on a randomly sampled subset of training points, utilizing the learned parameters independently of test data supervision.

**Coverage and reconstruction diagnostics.** Figure 7 illustrates three diagnostic views, each calculated for a different dataset (Fashion-MNIST, MNIST, and SIFT), to evaluate the accuracy of the Gaussian models in representing the datasets. The **top row** includes the *reconstruction landscape*, which visualizes the minimum Mahalanobis distance from each

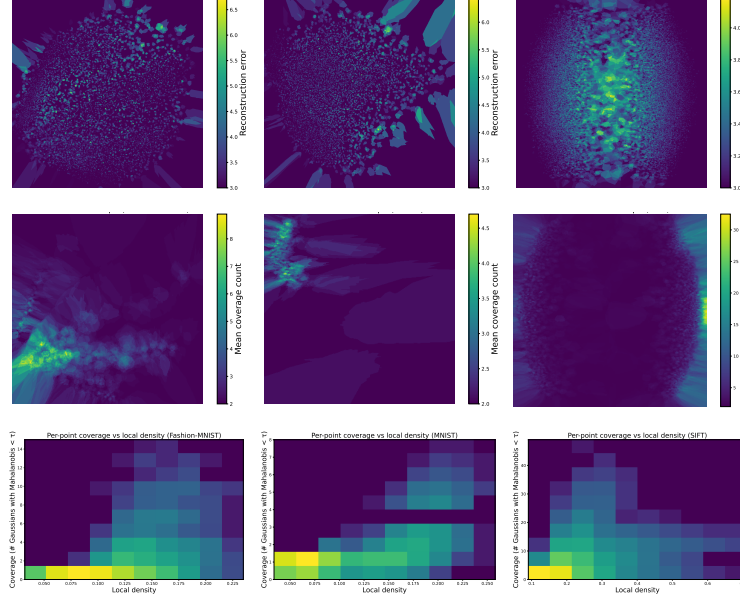


Figure 7: Diagnostic visualizations across Fashion-MNIST (left), MNIST (middle), and SIFT (right). Top row: minimum Mahalanobis reconstruction error; middle row: average Gaussian coverage per point; bottom row: relationship between local density and Gaussian coverage. Bottom row’s colormap depicts frequency-density, in logarithmic scale.

point to any Gaussian. For each dataset, we employ PCA to project the points onto a two-dimensional space and calculate the average reconstruction error of proximate points on a grid. This heatmap highlights how well the Gaussian shells approximate the distribution of data throughout the space.

The **middle row** shows the *coverage landscape*, which counts how many Gaussians fall within the Mahalanobis threshold  $\tau$  for each data point. Coverage is computed per point, projected to 2D, and smoothed via k-NN averaging over a grid. This plot reflects the redundancy and spatial spread of the Gaussian coverage. We observe that areas with low reconstruction error tend to have high coverage.

The **bottom row** depicts the *relationship between local density and Gaussian coverage*. For each point, we compute its local density via the inverse mean distance to its 10 nearest neighbors and correlate this with its coverage count. The resulting 2D histograms reveal structural patterns where regions of higher density generally exhibit greater coverage while sparse regions receive fewer assignments. This aligns with our goal of achieving balanced coverage while maintaining good reconstruction fidelity.

**Curvature-based diagnostics.** Fig. 8 provides four views exploring the relationship between curvature and structural properties of the Gaussian assignments across datasets, to examine whether the learned model is informative and geometrically consistent with the data  $x \in X$ .

The **first row** shows the standard deviation of local curvature as a function of the average radius ( $l_2$ ) per Gaussian. For each Gaussian, we collect nearby assigned points (under Mahalanobis threshold  $\tau$ ), compute their curvature via PCA-based local flatness, and report the standard deviation. Each bin aggregates Gaussians by radius and variation in curvature, highlighting the stability of their local geometry, where for each dataset curvatures deviations tend to be around  $\sim 0.06$ .

The **second row** reports the mean curvature of each Gaussian against its average radius. This indicates the intrinsic dimensionality and shape complexity of regions assigned to Gaussians of different spatial extent. In general, we see that mean curvature tends to be  $\sim 0.5$ , suggesting a moderate level of local non-linearity, especially for Gaussians with smaller

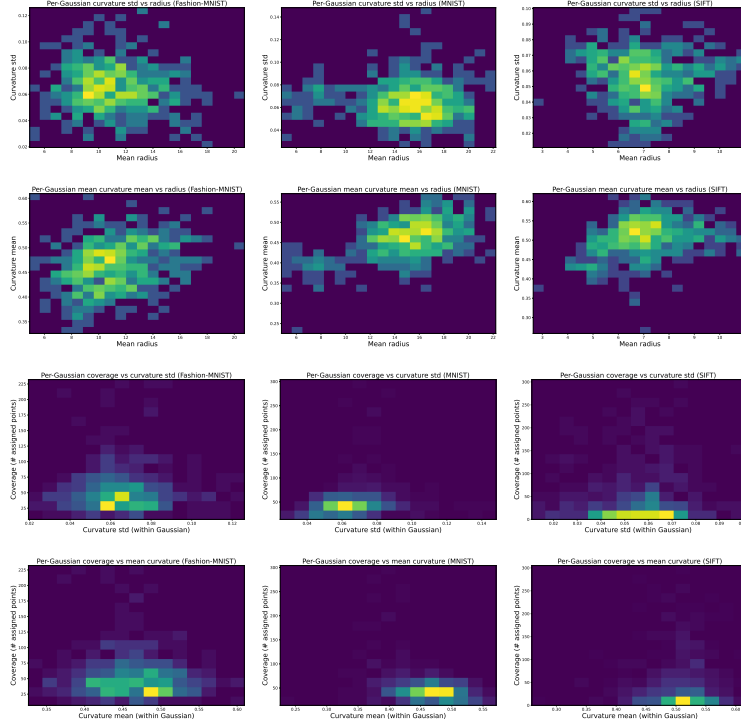


Figure 8: Curvature diagnostics across Fashion-MNIST (left), MNIST (middle), and SIFT (right). Row 1: standard deviation of local curvature vs radius; Row 2: mean local curvature vs radius; Row 3: Gaussian coverage vs curvature std; Row 4: Gaussian coverage vs curvature mean. Coloring accounts for density.

support. As the radius increases, curvature remains relatively stable, indicating consistent local geometry across scales.

The **third row** depicts how Gaussian coverage (number of assigned points) varies with the curvature standard deviation of the assigned region. We observe that most Gaussians exhibit low curvature variability ( $\text{std} \sim 0.06$ ), indicating that points within each Gaussian tend to have similar geometric structure. Moreover, there is no clear correlation between coverage and curvature std, implying that heavily used Gaussians are not more geometrically diverse than others. This suggests a form of balanced representation capacity across Gaussians.

The **fourth row** shows coverage as a function of mean curvature, where Gaussians with high coverage have curvature patterns similar to those with low coverage.

Fig. 9 demonstrates the capability of GARLIC to capture the intrinsic geometric structure of high-dimensional data with locally varying dimensionality. The anisotropy histograms (first row) reveal how Gaussians adapt to regions of different local dimensionality, with  $\lambda_{\max}/\lambda_{\min}$  ratios ranging from nearly isotropic to highly stretched configurations across all datasets. Rather than simply partitioning space uniformly, Gaussians adapt their shapes to the underlying manifold structure, as confirmed by the diagonality histograms (third row) and effective dimension measurements (fourth row). This representation allows us to model stratified data where different intrinsic dimensionalities coexist, allowing the data to become pancake-like for surface regions, needle-like for curve regions, and ball-like for volumetric areas. Unlike traditional space partitioning methods, GARLIC models the underlying data distribution probabilistically, not just approximating distances for retrieval. The explained variance surfaces (bottom row) show that Gaussians efficiently capture the relevant dimensions at each location, enabling estimation of true manifold distances rather than just Euclidean distances to samples. This provides more semantically meaningful results in regions where the intrinsic dimensionality is lower than the ambient space. This completes the supplementary material.

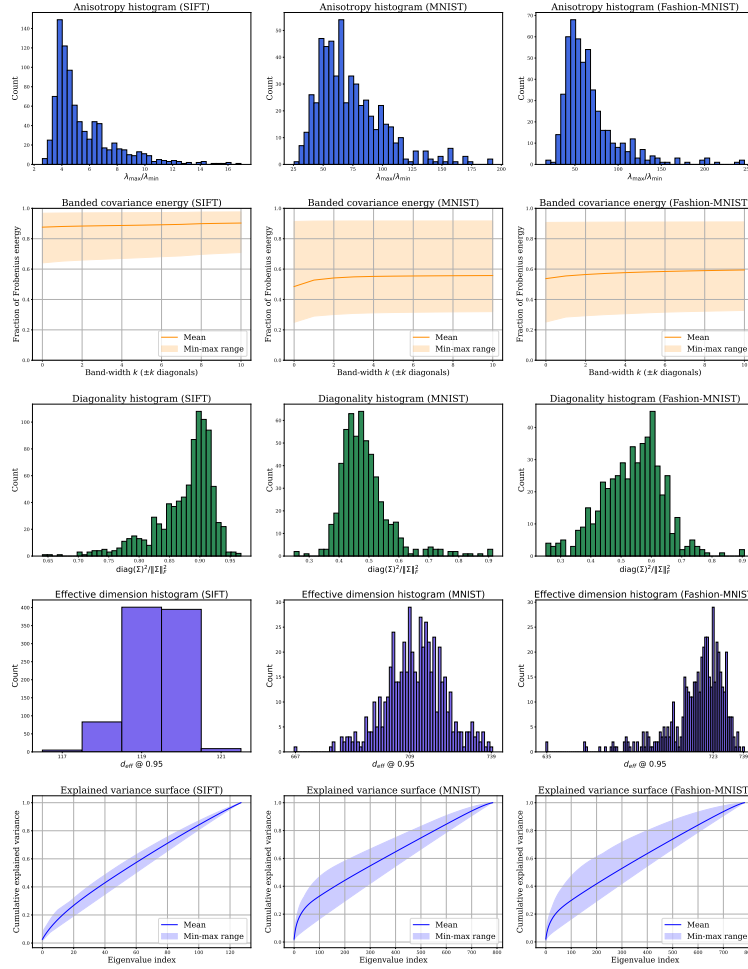


Figure 9: Spectral diagnostics across datasets (SIFT, MNIST, Fashion-MNIST; columns) and Gaussian properties (rows). Each subplot shows a different measure: anisotropy, band energy, diagonality, effective dimension, and explained variance.